

On the Impact of Channel Aging and Doppler-Affected Clutter on OFDM ISAC Systems

Steven Rivetti, *Student Member, IEEE*, Gabor Fodor, *Fellow, IEEE*
Emil Björnson, *Fellow, IEEE*, Mikael Skoglund, *Fellow, IEEE*

Abstract—The temporal evolution of the propagation environment plays a central role in integrated sensing and communication (ISAC) systems. A slow-time evolution manifests as channel aging in communication links, while a fast-time one is associated with structured clutter with non-zero Doppler. Nevertheless, the joint impact of these two phenomena on ISAC performance has been largely overlooked. This addresses this research gap in a network utilizing orthogonal frequency division multiplexing waveforms. Here, a base station simultaneously serves multiple user equipment (UE) devices and performs monostatic sensing. Channel aging is captured through an autoregressive model with exponential correlation decay. In contrast, clutter is modeled as a collection of uncorrelated, coherent patches with non-zero Doppler, resulting in a Kronecker-separable covariance structure. We propose an aging-aware channel estimator that uses prior pilot observations to estimate the time-varying UE channels, characterized by a non-isotropic multipath fading structure. The clutter’s structure enables a novel low-complexity sensing pipeline: clutter statistics are estimated from raw data and subsequently used to suppress the clutter’s action, after which target parameters are extracted through range-angle and range-velocity maps. We evaluate the influence of frame length and pilot history on channel estimation accuracy and demonstrate substantial performance gains over block fading in low-to-moderate mobility regimes. The sensing pipeline is implemented in a clutter-dominated environment, demonstrating that effective clutter suppression can be achieved under practical configurations. Furthermore, our results show that dedicated sensing streams are required, as communication beams provide insufficient range resolution.

Index Terms—Channel aging, clutter, ISAC, OFDM radar

I. INTRODUCTION

SIXTH-generation wireless networks are envisioned to support not only high-rate communications but also native sensing and environmental awareness. Integrated sensing and communications (ISAC) has emerged as a key enabling paradigm in which sensing and communication tasks cooperate rather than competing for the ever more scarce spectral resources. [1]. Among the many possible sensing topologies, monostatic sensing utilizing massive multiple-input multiple-output (MIMO) at cellular base station (BS) is of interest to the standardization and research communities due to its implementation advantages by utilizing large antenna arrays,

advanced signal processing capabilities, and readily making the communication signal available to the sensing receiver. In addition, cellular monostatic sensing does not require costly synchronization between multiple BSs [2] or between user equipment (UE) devices and BSs [3]. However, the monostatic operation sensing requires partitioning the antennas between transmission and reception, which differs from conventional communication-only deployments. Furthermore, to facilitate task integration, an ISAC system splits its available resources, such as transmit power and bandwidth, between the two tasks [4]. The allocation of these resources is the primary factor determining the trade-off between sensing and communication. Examples of optimal resource allocation aimed at achieving the optimal tradeoff can be found in [5], [6].

A fundamental design choice in ISAC systems is whether to pursue full integration between sensing and communication or to introduce some degree of separation between them. In this regard, [7] provides a tutorial on how sensing can be performed with a waveform optimized for communications, thus achieving maximum integration. However, this degree of integration introduces the so-called deterministic-random tradeoff: sensing benefits from deterministic signals while communication needs random ones. Introducing a degree of separation between the tasks can mitigate this tradeoff. In this regard, [8] shows how space separation, achieved through the allocation of dedicated sensing streams in addition to the communication ones, achieves better angle of arrival (AoA) estimation performance than a time separation scheme, where each task is carried out individually during different timeslots. It is also worth mentioning that the geographical separation between a target and the communication UEs might make task separation unavoidable [9], [10]. While sensing inherently relies on fast-time temporal variations of line of sight (LoS) channels, communication channels, which are usually dominated by their non-line-of-sight (NLoS) parts, show a slow-time temporal evolution caused by UEs mobility and environmental changes. This temporal evolution is often simplified through the adoption of a block-fading model, which assumes a block-wise constant channel with every block being an independent realization. Although mathematically appealing, this model fails to capture channel aging [11], directly impacting the communication performances. Channel aging can be modeled by accounting for statistical characteristics of the channel’s temporal [12], [13].

Furthermore, recent advances in receiver design and channel estimation/prediction in communication systems indicate that pilot spacing (frame size) can help mitigate the negative

This work was supported by the SUCCESS project (FUS21-0026), funded by the Swedish Foundation for Strategic Research. G. Fodor was supported by the Swedish Strategic Research (SSF) FUS21-0004 SAICOM project.

The authors are with the School of Electrical Engineering and Computer Science (EECS), KTH Royal Institute of Technology, 11428 Stockholm, Sweden. This work was carried out while the first author was an intern at Ericsson Research, Stockholm, Sweden. Gabor Fodor is also with Ericsson Research, Stockholm, Sweden.

effects of channel aging. This is a notoriously difficult problem to deal with: [14] derives an upper bound on the spectral efficiency (SE) of a single antenna UE, finding the pilot spacing dictating the optimal trade-off between channel state information (CSI) quality and SE. [15] extends the previous analysis to non-stationary aging Rician channels, designing a multi-frame structure for data transmission, finding the optimal pilot spacing and power control strategy. [16] studies how hardware impairments affect the optimal pilot spacing. A data-driven approach has been investigated in [17], where the temporal correlation pattern is extracted by a convolutional neural network and the CSI is predicted through an autoregressive (AR) network.

Somewhat surprisingly, the impact of channel aging on the communication performance of ISAC systems in general and monostatic ISAC systems in particular has not been fully investigated. In [18], a tracking-oriented approach is employed, where the aging time is defined as the number of blocks elapsed since the last pilot transmission, i.e., the number of blocks whose CSI relies solely on prediction. CSI is initially acquired through pilot transmission and minimum mean square error (MMSE) estimation, while prediction is achieved through a Kalman filter. In spite of the fact that clutter is an unavoidable aspect affecting any radar system, many previous works fail to address the clutter's temporal evolution and its extended nature. In [19], a beam-squint-based ISAC scheme is proposed, aimed at near-field monostatic operation in the terahertz frequency band. Here, clutter is defined as a static grid of point-like reflectors. Although mathematically appealing, this does not capture the temporal evolution and spatial structure of realistic clutter environments.

On the other hand, [20] allows for clutter to be composed of moving point-like scatterers, which nonetheless fails to account for the coherent, spatially extended structure of real clutter patches, which usually have non-negligible angular, Doppler, and delay spreads. Clutter suppression is critical to the performance of ISAC systems in terms of object detection and parameter estimation. For instance, [21] proposes an eigenvalue-based detection scheme applied to a narrow-band ISAC system, where the clutter space distribution is modeled as a set of patches and Toeplitz time-correlated noise. The same target detection problem in the presence of a patched cluster is tackled in [22]: here, the monostatic operation of a Reconfigurable intelligent surface (RIS) assisted ISAC network is analyzed, resulting in the proposal of a clutter distribution-agnostic target detector and a RIS phase-shift optimization algorithm.

In this paper, we argue that ignoring or oversimplifying clutter leads to the design of less useful sensing pipelines in ISAC systems. In light of these recent advances in the design of ISAC systems, we aim to analyze the impact of environmental changes on a monostatic ISAC network. The said network employs orthogonal frequency division multiplexing (OFDM) waveforms to perform monostatic sensing in an urban scenario. More specifically, our paper asks the following two important questions, which have not been conclusively answered by previous works:

- What is the impact of channel aging in an ISAC scenario

with multiple-antenna UEs? How can one leverage the known channel temporal correlation structure to one's advantage?

- What is a realistic yet mathematically tractable model for clutter in an urban scenario? How can one suppress the clutter action on the observed sensing data?

In light of these questions, the main contributions of our paper are the following:

- We model the spatial and time correlation of the BS-UE channels. Their spatial covariance matrix is characterized in Lemma 1, their temporal correlation follows a first-order AR process with Bessel correlation decay. Lemma 5 and its corollaries propose an aging-aware MMSE channel estimator.
- Inspired by airborne and synthetic aperture radar techniques [23], [24], We propose a Kronecker-separable clutter covariance model, which is novel within the ISAC environment. The clutter's covariance matrix is equal to the Kronecker product of the space, time, and frequency covariance matrices. Each of these matrices is defined in Lemma 2-4.
- A novel radar signal processing pipeline is proposed. Starting from the raw data, clutter's second-order statistics are estimated, which are then used to suppress the former's action. Finally, range-angle (RA) and range-velocity (RV) maps are computed.
- We numerically evaluate the performance of the proposed communication channel estimator and radar pipeline, showing their effectiveness.

The remainder of this article is organized as follows: Section II shows the system model of the investigated monostatic OFDM ISAC network. Section III provides the models for the UEs' channels space and time covariances as well as a full characterization of the clutter second-order statistics. Section IV presents the proposed aging-aware MMSE channel estimator, giving a statistical characterization of its channel estimate and channel estimation error. Section V presents the proposed radar signal processing pipeline, starting from the clutter covariance estimators in V-A. Section VI then shows the precoding techniques implemented in the article, consisting of MMSE precoders [25] for the communication streams and Communication null-space projected beamsweeping for the sensing stream. Finally, Section VII showcases the performance of the proposed channel estimator and radar pipeline.

Notation: Boldface lowercase and uppercase letters denote vectors and matrices, respectively. The trace of the matrix \mathbf{X} is denoted by $\text{Tr}(\mathbf{X})$. $\text{diag}(\mathbf{x})$ represents the stacking of \mathbf{x} on the main diagonal of a matrix. The creation of a tensor from a set of vectors is denoted by the following notation $\mathbf{Y} = \{\{\mathbf{y}_{1,c}, \dots, \mathbf{y}_{B,c}\}\}_{\forall c} \in \mathbb{C}^{A \times B \times C}$; conversely $\mathbf{y}_{b,c} = \{\mathbf{Y}\}_{b,c}$. The notation $\mathcal{CN}(0, \sigma^2)$ represents the circularly symmetric complex Gaussian distribution with variance σ^2 . Given the matrix $\mathbf{X} \in \mathbb{C}^{A \times B}$, the notation $\mathbf{Y} = \text{vec}(\mathbf{X}) \in \mathbb{C}^{AB}$ stacks the columns of said matrix to form a vector. The same applies to a tensor $\mathbf{X} \in \mathbb{C}^{A \times B \times C}$: $\mathbf{y} = \text{vec}(\mathbf{X}) \in \mathbb{C}^{ABC}$. Given the vector \mathbf{x} , the notation $\mathcal{T}(\mathbf{x})$ denotes the Toeplitz matrix built from \mathbf{x} . Given the tensor $\mathbf{Y} \in \mathbb{C}^{A \times B \times C}$, the notation $\mathbf{X} =$

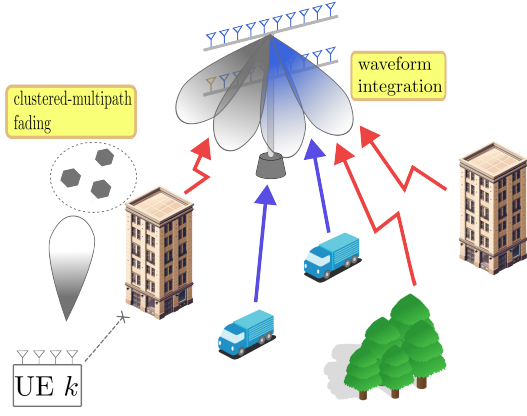


Fig. 1: A single-cell network, where the BS uses multi-antenna transmission to provide ISAC services. This downlink signal is used to transmit pilots for channel estimation [26] and as a radar probe for monostatic sensing [27]. The blue arrows represent target echoes, whereas the red arrows represent ground clutter echoes.

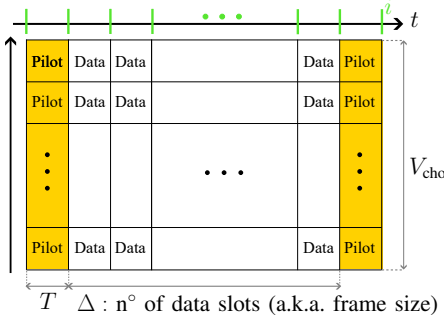


Fig. 2: Representation of the pilot and data symbols transmission structure in the time-frequency domain. This transmission occurs on the communication channel, which is estimated at the start of each pilot slot.

$\mathcal{U}_1(\mathbf{Y})$ denotes the unfolding of \mathbf{Y} along the first dimension, resulting in the matrix $\mathbf{X} \in \mathbb{C}^{A \times BC}$. On the other hand, given the same matrix \mathbf{X} , mentioned above, $\mathbf{Y} = \mathcal{F}_1(\mathbf{X})$ denotes the folding operation, retrieving the original tensor.

II. SYSTEM MODEL

We consider the single-cell scenario shown in Figure 1, where a BS, equipped with M_{BS} receiving and transmitting antennas, serves K communication UE devices, equipped with M_{UE} antennas. The downlink (DL) channels between the BS and the UEs are estimated by transmitting DL pilot signals and assuming instantaneous feedback by the UEs. At the same time, the transmitted waveform is used as a radar probing signal to calculate the positions and velocities of L targets in a monostatic manner. The system implements OFDM transmission around carrier frequency f_c , over V active subcarriers with a subcarrier spacing of Δ_f . Here $T = 1/\Delta_f + T_{cp}$ is the symbol duration, with T_{cp} being the cyclic prefix duration. The communication channel between the BS and UE k at time t is denoted by $\mathbf{H}_{k,t} \in \mathbb{C}^{M_{UE} \times M_{BS}}$. Due to the assumed frequency-domain block-fading structure, we omit the subcarrier index from \mathbf{H}_k : the modeling considerations in the sequel refer to an arbitrary coherence block. Under these assumptions, let us build the vectorized channel of

the k -th UE, denoted by $\mathbf{h}_{k,t} = \text{vec}(\mathbf{H}_{k,t}) \in \mathbb{C}^{M_{BS}M_{UE}}$, by stacking the columns of $\mathbf{H}_{k,t}$. The vectorized channel follows a correlated Rayleigh fading distribution, where the covariance matrix follows a Kronecker model [28]: this model is a good fit since the UE and BS are in the respective far fields and the multipath is originated by a set of communication clusters. A communication cluster (referred to as “cluster” in the sequel) is defined as a set of closely spaced scatterers in the proximity of the UE, generating small-scale fading [29]. Therefore, $\mathbf{h}_{k,t} \sim \mathcal{CN}(\mathbf{0}, \mathbf{C}_k)$, where

$$\mathbf{C}_k = \mathbf{C}_{Tx,k} \otimes \mathbf{C}_{Rx,k} \in \mathbb{C}^{M_{BS}M_{UE} \times M_{BS}M_{UE}}. \quad (1)$$

Here, $\mathbf{C}_{Tx,k} \in \mathbb{C}^{M_{BS} \times M_{BS}}$, and $\mathbf{C}_{Rx,k} \in \mathbb{C}^{M_{UE} \times M_{UE}}$ are the transmitter and receiver side correlation matrices respectively. We further assume that $\{\mathbf{H}_{k,t}\}_{\forall k}$ follows an aging structure in time, a model that aims to leverage the channel’s correlation between timeslots, a degree of freedom not exploited when a block fading channel structure is assumed [30]. We model this time aging as a first-order AR process. Since each spatial component undergoes the same channel aging, the AR process state transition matrix is a scaled identity matrix [14], [31], where the scaling component controls the correlation decay over time. Under these assumptions, the correlation between $\mathbf{h}_{k,t}$ and $\mathbf{h}_{k,t+iT}$ is defined as

$$\mathbb{E}[\mathbf{h}_{t,k} \mathbf{h}_{t+iT,k}^H] = \mathbf{C}_k \zeta_k(iT), \quad (2)$$

where $\zeta_k(iT)$ captures the correlation decay in time slot i . Without loss of generality and for the sake of clarity, this notation assumes that the time unit is T and therefore we will write $iT = i$ in the sequel. Let us collect the channel realizations of Δ time slots in the vector $\mathbf{h}_k \in \mathbb{C}^{M_{BS}M_{UE}\Delta}$. This is a zero-mean complex Gaussian vector whose covariance matrix is defined as

$$\mathbb{E}[\mathbf{h}_k \mathbf{h}_k^H] = \mathbf{C}_k \otimes \mathcal{T}([\zeta_k(0), \dots, \zeta_k(\Delta)]). \quad (3)$$

The frequency-domain sensing channel at subcarrier v , denoted by $\mathbf{G}_{i,v} \in \mathbb{C}^{M_{BS} \times M_{BS}}$, is defined as

$$\mathbf{G}_{i,v} \triangleq \sum_{l=1}^L \alpha_l e^{-j2\pi f_{D,l} T i} e^{j2\pi \Delta_f v \tau_l} \mathbf{a}(\theta_l) \mathbf{a}(\theta_l)^H, \quad (4)$$

where $\tau_l, \theta_l, f_{D,l}$ are the two-way time-delay, the AoA, and the Doppler shift of the target, respectively. The Doppler shift of target l is computed as $f_{D,l} = 2\nu_l/\lambda_c$, with ν_l representing the target’s radial velocity. We assume that the target position changes much more slowly than the communication channel; indeed, its parameters are assumed to be constant for at least I OFDM symbols. The BS is positioned in the origin, whereas the l -th target’s position is denoted by $\mathbf{p}_l = [p_{x,l}, p_{y,l}]^T$; it then follows that $\theta_l = \text{atan2}(p_{y,l}, p_{x,l})$, $\tau_l = 2r_l/c$, $r_l = \|\mathbf{p}_l\|$. Under the narrow-band assumption $\lambda_c \approx \lambda_v$, and the steering vector is defined as $\mathbf{a}(\theta_l) \triangleq [e^{-j\pi(-\frac{M_{BS}}{2}) \sin(\theta_l)} \dots e^{-j\pi(\frac{M_{BS}}{2}-1) \sin(\theta_l)}]^T$. The coefficient α_l is the complex channel gain of target l , which is defined as

$$\alpha_l = \sqrt{\frac{G_{Tx} G_{Rx} c^2 \delta_{v,l}^2}{(4\pi)^3 f_c^2 r_l^4}} e^{j2\pi f_c \tau_l}. \quad (5)$$

Here, G_{Tx} , G_{Rx} are the single-element transmit and receive antenna gains and $\delta_{\text{lg},l}^2$ represents l -th target radar cross section (RCS). As mentioned in the introduction, in real ISAC scenarios, the target parameters need to be recovered in an environment dominated by clutter [32]. In the radar literature, clutter is defined as the spurious returns originating from the environment surrounding the targets. If not handled properly, clutter causes great harm to the radar system [24]. We model clutter as an additive colored complex Gaussian noise term, denoted by $\mathbf{c}_{i,v}$, and notice that if we were to collect the clutter terms on all subcarriers and timeslots in $\mathbf{c} = [\mathbf{c}_{1,1}^\top, \dots, \mathbf{c}_{I,V}^\top]^\top$, this would be distributed as $\mathbf{c} \sim \mathcal{CN}(\mathbf{0}, \delta_{\text{cl}}^2 \mathbf{B})$. Here, δ_{cl}^2 represents the clutter's power, which is usually referred to as the clutter's texture. In spherically-invariant random vector clutter models, this parameter follows a heavy-tailed distribution (e.g., Weibull) as it represents slow variations of the clutter energy [33]. We set this parameter to a constant value, typically referred to as homogeneous clutter. This choice preserves the Gaussianity of \mathbf{c} , making the subsequent mathematical derivations more tractable and insightful. The transmitted waveform during a generic data-timeslot i at subcarrier v is defined as

$$\mathbf{s}_{i,v} = \sum_{s=1}^S \underbrace{\mathbf{f}_{i,v,s} \sqrt{\rho_{i,v,s}} x_{i,v,s}}_{\mathbf{s}_{i,v,s}} = \mathbf{F}_{i,v} \mathbf{P}_{i,v} \mathbf{x}_{i,v} \in \mathbb{C}^{M_{\text{BS}}}, \quad (6)$$

where $\mathbf{P}_{i,v} = \text{diag}(\rho_{i,v})$ and $\mathbf{F}_{i,v} \in \mathbb{C}^{M_{\text{BS}} \times S}$ represents the precoding matrix. We allocate M_{UE} streams to each UE and an additional one for sensing purposes. The precoding matrix associated to UE k is $\mathbf{F}_{i,v,k} = [\mathbf{f}_{i,v,k,1}, \dots, \mathbf{f}_{i,v,k,M_{\text{UE}}}] \in \mathbb{C}^{M_{\text{BS}} \times M_{\text{UE}}}$, thus making the total precoding matrix equal to

$$\mathbf{F}_{i,v} \triangleq [\mathbf{F}_{i,v,1}, \dots, \mathbf{F}_{i,v,K}, \mathbf{f}_{i,v,S}] \in \mathbb{C}^{M_{\text{BS}} \times S}. \quad (7)$$

We assume that each column of that matrix is normalized to have a unitary norm. We denote by $\rho_{i,v,s}$ the power assigned by the BS to the s -th stream on subcarrier v at time i . More specifically $\boldsymbol{\rho}_{i,v} \triangleq [\rho_{i,v,1}^\top \dots \rho_{i,v,K}^\top \sqrt{\rho_{i,v,S}}]^\top$, with $\rho_{i,v,k} = [\sqrt{\rho_{i,v,k,1}} \dots \sqrt{\rho_{i,v,k,M_{\text{UE}}}}]^\top$. The total power budget P_{Tx} of the BS is divided between sensing and communication and sensing beams, where the individual power budgets are denoted by P_{comm} and P_{sens} . The BS employs the entirety of its power budget during each timeslot i , thus P_{comm} and P_{sens} can be defined as

$$P_{\text{comm}} = \sum_{s=1}^{KM_{\text{UE}}} \sum_{v=1}^v \rho_{i,v,s} = P_{\text{Tx}} \gamma, \quad \forall i, \quad (8)$$

$$P_{\text{sens}} = \sum_{v=1}^v \rho_{i,v,S} = P_{\text{Tx}} (1 - \gamma), \quad \forall i. \quad (9)$$

Here, γ regulates the power allocation, embodying the inherent power trade-off between sensing and communications. At time instance i , the transmitted symbols on subcarrier v , either pilots or information-bearing symbols, are defined as

$$\mathbf{x}_{i,v} = [\mathbf{x}_{i,v,1}^\top, \dots, \mathbf{x}_{i,v,K}^\top, x_{v,i,S}]^\top \quad (10)$$

where $\mathbf{x}_{i,v,k} \in \mathbb{C}^{M_{\text{UE}}}$ is the vector of symbols meant for UE k and $x_{i,v,S} \sim \mathcal{CN}(0, 1)$. The frequency-domain observation

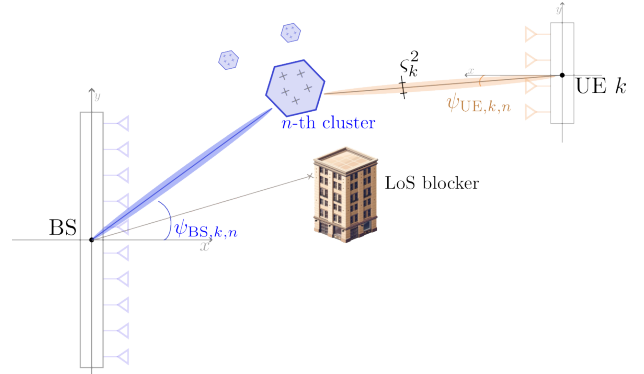


Fig. 3: Clustered multipath transmission geometry of the channel between the BS and UE k . Both covariances $\mathbf{C}_{\text{Tx},k}$ and $\mathbf{C}_{\text{Rx},k}$ originate from the same set of clusters, albeit seen from different angles.

at UE k during a generic data slot i at subcarrier v is defined as

$$\mathbf{y}_{i,v,k} \triangleq \alpha_k \mathbf{H}_{i,k} \mathbf{s}_{i,v} + \mathbf{n}_{i,v,k} \in \mathbb{C}^{M_{\text{UE}}}, \quad (11)$$

where $\mathbf{n}_{i,v,k}$ is the receiver noise at UE k at timeslot i and subcarrier v , whose entries independent identically distributed (i.i.d.) random variables distributed as $\mathcal{CN}(0, \sigma_k^2)$. On the other hand, during any timeslot i , the observed radar echo at the BS can be defined as

$$\mathbf{y}_{i,v} \triangleq \boldsymbol{\mu}_{i,v} + \mathbf{c}_{i,v} + \mathbf{n}_{i,v}^r \in \mathbb{C}^{M_{\text{BS}}}. \quad (12)$$

where $\boldsymbol{\mu}_{i,v} = \mathbf{G}_{i,v} \mathbf{s}_{i,v}$ represents the noiseless and clutterless observation. Once again, $\mathbf{n}_{i,v}^r$ is the radar receiver noise at timeslot i and subcarrier v , whose entries are i.i.d. random variables distributed as $\mathcal{CN}(0, \sigma^2)$.

III. CHARACTERIZING THE IMPACT OF CHANNEL AGING AND CLUTTER

In this section, we characterize the covariances of the communication channels and the observed clutter. Fig. 3 shows how the spatial covariance matrix of $\mathbf{h}_{i,k}$ follows a non-isotropic multipath model, as a set of clusters originates the multipath. Similarly, Fig. 4 shows how clutter is generated by approximately independent clutter patches, each contributing to the total covariance. Recall that a clutter patch refers to a region of the environment that produces radar echoes that approximately have the same angle, Doppler shift, and range; indeed, we assume that the spreads describing the patch (i.e., angle, Doppler, and delay spread) are small.¹

A. Spatial and Temporal Covariances of UE Channels

We will now focus on the computation of the transmit-side correlation $\mathbf{C}_{\text{Tx},k}$, as the procedure to retrieve $\mathbf{C}_{\text{Rx},k}$ is entirely analogous. In its most general form, we may write that

$$\mathbf{C}_{\text{Tx},k} = \int_{-\frac{\pi}{2}}^{\frac{\pi}{2}} f_k(\psi) \mathbf{a}(\psi) \mathbf{a}(\psi)^H d\psi, \quad (13)$$

¹Although clutter patches and communication clusters are described by the same mathematical model, they represent different physical scales. Specifically, the former represents extended surfaces while the latter captures the effect of small-scale scatterers close to the UE: for this reason, the set of clusters creating \mathbf{C}_k does not constitute a clutter patch.

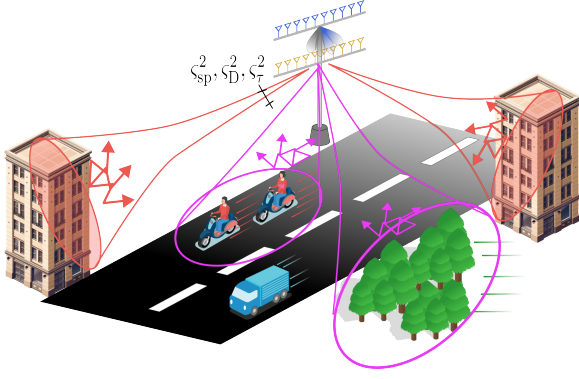


Fig. 4: Visual representation of the clutter environment. Clutter is formed by a discrete number of clutter patches, both static and dynamic, which can be approximated with a median angle, Doppler shift, and delay.

where $f(\psi)$ is the angular spreading function, which specifies the gain and phase shifts associated with every angular direction. A visual representation of the gain angular distribution is provided in Fig. 3. We can see that the LoS between BS and UE k is blocked and the signal transmitted by the BS reaches the UE through a set of N_k scatterers [34]. The angular spreading function can be modeled as [35]

$$f_k(\psi) = \frac{1}{N_k} \sum_{n=1}^{N_k} \frac{1}{\sqrt{2\pi}\zeta_k} \exp\left\{-\frac{(\psi - \psi_{BS,k,n})^2}{2\zeta_k^2}\right\}, \quad (14)$$

where $\psi_{BS,k,n}$ is the n -th cluster's angle as seen from the BS: all the clusters are within an angular interval $\Delta\psi_{BS,k,n}$. Each scatterer reflects the impinging signal with an angular spread of ζ_k^2 .

Lemma 1. *Under the assumption of small angular spreads i.e., $\cos(\zeta_k) \approx 1$ and $\sin(\zeta_k) \approx \zeta_k$, each entry of $\mathbf{C}_{Tx,k}$ can be tightly approximated as*

$$[\mathbf{C}_{Tx,k}]_{l,m} \approx \sum_{n=1}^N \frac{A_{l,m}(\psi_{BS,k,n})}{N_k} e^{-\frac{\pi^2}{2}((l-m)\cos(\psi_{BS,k,n})\zeta_k)^2} \quad (15)$$

where $l, m = 1, \dots, M_{BS}$, and $A_{l,m}(\psi_{BS,k,n}) = e^{-j\pi(l-m)\sin(\psi_{BS,k,n})}$.

Proof: A proof and tightness analysis of this approximation can be found in [36, Lemma 2]. ■

The temporal evolution (aging) of the channel is modeled as a first-order AR process with a scale-identity state-transition matrix. The scaling coefficient $\zeta_k(i)$ representing the correlation decay is chosen as $\zeta_k(i) = J_0(2\pi T f_{D,k}^{UE} i)$, where $f_{D,k}^{UE}$ is UE k 's Doppler shift and $J_0(\cdot)$ is the zero-th order Bessel function [37]. The dependence of ζ_k on $f_{D,k}^{UE}$ is motivated by the latter's direct impact on the coherence time of \mathbf{h}_k , thus constituting a good indication of the time correlation decay.

B. Clutter Characterization

Recall that clutter originates from a few strong patches (Fig. 4), creating reflected echoes with “narrow” lobes. Under this

assumption, the clutter covariance matrix can be approximated as

$$\mathbb{E}[\mathbf{c}\mathbf{c}^H] = \delta_{cl}^2 \mathbf{B} \approx \sqrt[3]{\delta_{cl}^2} \mathbf{B}_{sp} \otimes \sqrt[3]{\delta_{cl}^2} \mathbf{B}_t \otimes \sqrt[3]{\delta_{cl}^2} \mathbf{B}_r \quad (16)$$

This model is widely studied in the radar literature and is referred to as the Kronecker-separable clutter model [23]. Here, \mathbf{B}_{sp} , \mathbf{B}_t , and \mathbf{B}_r model the clutter's angle, Doppler, and range distribution. The main advantage of this model is its low computational complexity, stemming from the fact that operations such as whitening, eigen-decomposition, and inversion can be applied independently to each dimension. The space covariance \mathbf{B}_{sp} is computed in the same way as in (15), as clutter patches and UE clusters have the same mathematical model.

Lemma 2. *Let us denote the clusters angular spread as ζ_{sp} . Under the assumption of almost independent patches and of small angular spreads, i.e. $\cos(\zeta_{sp}) \approx 1$ and $\sin(\zeta_{sp}) \approx \zeta_{sp}$, each entry f \mathbf{B}_{sp} is approximated by*

$$[\mathbf{B}_{sp}]_{l,m} \approx \frac{1}{N} \sum_{n=1}^N A_{l,m}(\psi_n) e^{-\frac{1}{2}(\pi(l-m)\cos(\psi_n)\zeta_{sp})^2} \quad (17)$$

where $l, m = 1, \dots, M_{BS}$, and $A_{l,m}(\psi_n) = e^{-j\pi(l-m)\sin(\psi_n)}$.

Proof: The proof of this lemma is analogous to the proof of Lemma 1 and is thus omitted. ■

The role of the temporal covariance matrix differs from that in communication-oriented analyses. In radar applications, the matrix \mathbf{B}_t captures the clutter's Doppler signature, allowing for distinguishing it from the target's. For this reason, \mathbf{B}_t is computed similarly to \mathbf{B}_{sp} . Let us start by defining each element \mathbf{B}_t as the inverse Fourier transform of the power spectral density

$$\mathbf{B}_t = \int_{-\infty}^{+\infty} g(f) \mathbf{b}(f) \mathbf{b}(f)^H df, \quad (18)$$

where $\mathbf{b}(f)$ is the Doppler steering vector $\mathbf{b}(f) = [1 \ e^{-j2\pi f D_n T} \ \dots \ e^{-j2\pi f T(I-1)}]^T \in \mathbb{C}^I$. Here, $g(f)$ is the power spectral density function, specifying the gain associated with each frequency component. Once again, this function is modeled as the summation of independent patches, that is

$$g(f) = \frac{1}{N} \sum_{n=1}^N \frac{1}{\sqrt{2\pi}\zeta_D} \exp\left\{-\frac{(f - f_{D,n})^2}{2\zeta_D^2}\right\}. \quad (19)$$

Here, $f_{D,n}$ is the n -th patch Doppler shift and ζ_D^2 is the Doppler spread. The clutter's Doppler spread ζ_D can be further expanded into $\zeta_D = 1/2\pi T I_c$, where I_c represents the number of OFDM symbols for which the clutter time correlation is greater than 0.

Lemma 3. *Under the assumption of almost independent patches, each entry of \mathbf{B}_t is computed as*

$$[\mathbf{B}_t]_{l,m} = \frac{1}{N} \sum_{n=1}^N D_{l,m}(f_{D,n}) e^{-\frac{(l-m)^2}{2I_c^2}}, \quad (20)$$

where $l, m = 1, \dots, I$, and $D_{l,m}(f_{D,n}) = e^{-j2\pi f_{D,n} T(l-m)}$.

Proof: Let us substitute (19) into (18) to obtain $[\mathbf{B}_t]_{l,m} = \frac{1}{N} \sum_{n=1}^N \int_{-\infty}^{+\infty} \frac{1}{\sqrt{2\pi\varsigma_D}} \exp\left\{-\frac{(f-f_{D,n})^2}{2\varsigma_D^2}\right\} e^{-j2\pi fT(l-m)} df$. By applying the square completion method and taking out of the integrals the terms constant in f , we can then rewrite the previous expression as

$$[\mathbf{B}_t]_{l,m} = \frac{1}{N} \sum_{n=1}^N e^{-j2\pi f_{D,n}T(l-m)} e^{-2(\pi T(l-m)\varsigma_D)^2} \times \int_{-\infty}^{+\infty} \frac{1}{\sqrt{2\pi\varsigma_D}} e^{-\frac{(f-f_{D,n}-j2\pi\varsigma_D^2T(l-m))^2}{\varsigma_D^2}} df. \quad (21)$$

The last integral integrates to 1 as $\varsigma_D > 0$, by substituting $\varsigma_D = 1/2\pi T I_c$ the expression follows. ■

The frequency covariance matrix is the Fourier transform of the power-delay spectrum

$$\mathbf{B}_f = \int_{-\infty}^{+\infty} h(\tau) \mathbf{d}(\tau) \mathbf{d}(\tau)^H d\tau, \quad (22)$$

where $\mathbf{d}(\tau)$ is the delay steering vector, defined as $\mathbf{d}(\tau) = [1 \ e^{j2\pi\Delta_f\tau} \ \dots \ e^{2\pi\Delta_f\tau(V-1)}]^\top \in \mathbb{C}^V$. Here, $h(\tau)$ is the power delay profile, associating a gain to a delay. Unlike a target, each clutter patch is an extended surface composed of multiple scatterers; this spoils the range coherence of each cluster, as the surface creates a diffusive reflection. The back-scattered echo from each of these patches is also affected by multipath. For this reason, in addition to a coherent term similar to the previously shown ones, $h(\tau)$ contains an additional term, denoted by $\tilde{h}(\tau)$, representing multipath and diffusive reflections. The power delay profile is thus defined as

$$h(\tau) = \frac{1}{N} \sum_{n=1}^N \frac{1}{\sqrt{2\pi\varsigma_\tau}} \exp\left\{-\frac{(\tau - \tilde{\tau}_n)^2}{2\varsigma_\tau^2}\right\} + \tilde{h}(\tau), \quad (23)$$

where $\tilde{\tau}_n$ is the median range of the n -th patch and $\tilde{\tau}_n = 2\tilde{r}_n/c$. Because of this modeling choice $\mathbf{B}_f = \bar{\mathbf{B}}_f + \tilde{\mathbf{B}}_f$. Let us denote with ς_τ^2 the patch's delay spread, to obtain:

Lemma 4. *Under the assumption of almost independent patches, each entry of \mathbf{B}_f is computed as*

$$[\bar{\mathbf{B}}_f]_{l,m} = \frac{1}{N} \sum_{n=1}^N E_{l,m}(\tilde{r}_n) e^{-2(\pi\Delta_f(l-m)\varsigma_\tau)^2} \quad (24)$$

$$\tilde{\mathbf{B}}_f = \chi \mathcal{T} \left(1 \ \mu_f^{\frac{\Delta_f}{B_{\text{cho}}}} \ \dots \ \mu_f^{\frac{(V-1)\Delta_f}{B_{\text{cho}}}} \right) \quad (25)$$

where $l, m = 1, \dots, V$, and $E_{l,m}(\tilde{r}_n) = e^{j2\pi\Delta_f \frac{2\tilde{r}_n}{c} (l-m)}$.

Proof: $\bar{\mathbf{B}}_f$ is obtained as in Lemma 3. On the other hand, we assume that the progression along τ of $\tilde{h}(\tau)$ follows an AR1 structure, making its contribution to \mathbf{B}_f a Toeplitz matrix [38]. ■

Here, $\tilde{\mathbf{B}}_f$ is characterized by $\mu_f < 1$, which is the correlation's decay magnitude, the coherence bandwidth B_{cho} , and χ , which is the power of the diffusive clutter w.r.t. the coherent one.

IV. COMMUNICATION CHANNEL ESTIMATION

We now provide a channel estimator for the communication channel. We adopt the simplifying assumption that the BS has an instantaneous feedback link from the UE regarding its channel estimate, allowing for channel state information at the transmitter (CSIT) in addition to channel state information at the receiver (CSIR). This is practically achieved by scheduling an additional uplink pilot slot after the downlink one [39]; we reserve the implementation of UL pilots for future work. It is also important to mention that the UE's time and space covariance matrices are assumed to be known. Each UE is associated with an S -stream pilot matrix denoted by $\mathfrak{J}_k \in \mathbb{C}^{S \times \tau_p}$. The first τ_p subcarriers of each coherence block are used to estimate the UEs' channels. We assume that during pilot transmission, the BS uses the same precoding matrix for all the subcarriers within the same block; we can thus drop the v index for the rest of this sub-section and derive the channel estimator of an arbitrary coherence block. Let us consider the arbitrary pilot slot ι , the signals received by UE k on all the τ_p subcarriers used for channel estimation can be written as

$$\mathbf{Y}_{k,\iota} = \alpha_k \mathbf{H}_{\iota,k} \mathbf{F}_\iota \mathbf{P}_\iota \sum_{k=1}^K \mathfrak{J}_k + \mathbf{N}_\iota \in \mathbb{C}^{M_{\text{UE}} \times \tau_p}, \quad (26)$$

where $\mathbf{N}_\iota = [\mathbf{n}_{\iota,1}, \dots, \mathbf{n}_{\iota,\tau_p}]$. To prevent pilot contamination, $\{\mathfrak{J}_k\}_{v_k}$ must satisfy $\mathfrak{J}_k \mathfrak{J}_{k'}^H = \tau_p \mathbf{I}_S \leftrightarrow k = k'$ and 0 otherwise; this can be achieved when $\tau_p \geq SK$. Precoded transmission during channel estimation is adopted to reduce the minimum τ_p , since without precoding $\tau_p \geq M_{\text{BS}}K$ [40]. Each UE de-spreads this observation as

$$\tilde{\mathbf{Y}}_{k,\iota} \triangleq \mathbf{Y}_{k,\iota} \mathfrak{J}_k^H / \sqrt{\tau_p} = \alpha_k \sqrt{\tau_p} \mathbf{H}_{\iota,k} \mathbf{F}_\iota \mathbf{P}_\iota + \tilde{\mathbf{N}}_{\iota,k}, \quad (27)$$

where $\tilde{\mathbf{N}}_{\iota,k} = \mathbf{N}_{\iota,k} \mathfrak{J}_k^H \in \mathbb{C}^{M_{\text{UE}} \times S}$. Let us introduce

$$\tilde{\mathbf{y}}_{\iota,k} = \text{vec}(\tilde{\mathbf{Y}}_{\iota,k}) = \alpha_k \sqrt{\tau_p} \check{\mathbf{F}}_\iota \mathbf{h}_{\iota,k} + \tilde{\mathbf{n}}_{\iota,k} \in \mathbb{C}^{SM_{\text{UE}}}, \quad (28)$$

where $\check{\mathbf{F}}_\iota = (\mathbf{F}_\iota \mathbf{P}_\iota)^\top \otimes \mathbf{I}_{M_{\text{UE}}} \in \mathbb{C}^{SM_{\text{UE}} \times M_{\text{UE}} M_{\text{BS}}}$ and $\tilde{\mathbf{n}}_{\iota,k} = \text{vec}(\tilde{\mathbf{N}}_{\iota,k})$. The estimate of the channel at the receiver can be based on multiple pilot observations before the actual data slot i . We assume that the receiver uses a total of p pilot observations before the present one, bringing the total number of observations to $p_{\text{tot}} = p + 1$, which are encompassed in

$$\tilde{\mathbf{y}}_k^{p_{\text{tot}}} = [\tilde{\mathbf{y}}_{\iota,k}^\top, \dots, \tilde{\mathbf{y}}_{\iota-(p_{\text{tot}}-1),k}^\top]^\top \in \mathbb{C}^{SM_{\text{UE}} p_{\text{tot}}}. \quad (29)$$

The following lemma shows how a channel estimate of $\mathbf{H}_{i,k}$, with ι being the closest pilot, is obtained.

Lemma 5. *The MMSE channel estimate of $\mathbf{h}_{i,k}$ given the pilot spacing Δ is obtained as*

$$\hat{\mathbf{h}}_{i,k} = \mathbf{A}_{i,k} \tilde{\mathbf{y}}_k^{p_{\text{tot}}} \in \mathbb{C}^{M_{\text{BS}} M_{\text{UE}}}, \quad (30)$$

where

$$\mathbf{A}_{i,k} = \alpha_k \sqrt{\tau_p} \mathbf{E}_{i,k} \check{\mathbf{F}}_{p_{\text{tot}}}^H \bar{\mathbf{A}}_{i,k}^{-1} \quad (31)$$

$$\bar{\mathbf{A}}_{i,k} = \alpha_k^2 \tau_p \check{\mathbf{F}}_{p_{\text{tot}}} \mathbf{M}_i \check{\mathbf{F}}_{p_{\text{tot}}}^H + \sigma_k^2 \mathbf{I}_{p_{\text{tot}} S M_{\text{UE}}} \quad (32)$$

$$\check{\mathbf{F}}_{p_{\text{tot}}} = \text{blkdiag} \left(\check{\mathbf{F}}_\iota, \dots, \check{\mathbf{F}}_{\iota-(p_{\text{tot}}-1)(\Delta+1)} \right) \quad (33)$$

$$\mathbf{E}_{i,k} = \mathbf{C}_k \otimes [\zeta_k(\bar{i}), \dots, \zeta_k(\bar{i} + (p_{\text{tot}} - 1)(\Delta + 1))], \quad (34)$$

$$\mathbf{M}_i = \mathbf{C}_k \otimes \mathcal{T}([\zeta_k(0), \dots, \zeta_k((p_{\text{tot}} - 1)(\Delta + 1))]), \quad (35)$$

and $\bar{i} = i - \iota$.

Proof: This can be obtained through standard MMSE estimator derivations by following the procedure in [14, Lemma 1]. ■

We move on to characterizing the distribution of the channel estimate

Corollary 1 . *The channel estimate $\hat{\mathbf{h}}_{i,k}$ is a zero-mean complex Gaussian random vector $\hat{\mathbf{h}}_{i,k} \sim \mathcal{CN}(\mathbf{0}, \hat{\mathbf{\Sigma}}_{i,k})$, where*

$$\hat{\mathbf{\Sigma}}_{i,k} = \alpha_k \tau_p \mathbf{E}_{i,k} \bar{\mathbf{A}}_{i,k}^{-1} \mathbf{E}_{i,k}^H \in \mathbb{C}^{M_{BS} M_{UE} \times M_{BS} M_{UE}}. \quad (36)$$

Stemming from Lemma 5 and Corollary 1 , we can now characterize the channel estimation error.

Corollary 2. *The channel estimation error $\tilde{\mathbf{h}}_{i,k} = \hat{\mathbf{h}}_{i,k} - \mathbf{h}_{i,k}$ is a complex Gaussian zero-mean vector whose covariance matrix can be defined as*

$$\tilde{\mathbf{\Sigma}}_{i,k} = \mathbf{C}_k - \hat{\mathbf{\Sigma}}_{i,k} \in \mathbb{C}^{M_{BS} M_{UE} \times M_{BS} M_{UE}} \quad (37)$$

V. RADAR SIGNAL PROCESSING

This section aims to give a practical radar signal processing pipeline, where, starting from the sensing observation,² the BS can estimate the parameters of each target. The first step is the estimation of the clutter's second-order statistics, so that the action of the former can be eliminated: this is carried out by leveraging the assumed sparsity in each dimension. Secondly, the action of the transmitted symbols is eliminated through clutter-aware matched filter (MF). The cleaned data is then used to compute RA and RV maps associated with every stream. Thanks to the slowly-changing target assumption, I timeslots are used for radar signal processing tasks. Once the maps have been obtained, estimation and detection should be applied to them [27]; we reserve their implementation for future work.

A. Clutter Covariance Estimator

Another strength of the Kronecker-separable covariance model is the ability to estimate each component separately, thereby reducing the overall computational complexity. Each covariance component's sparsity enables us to efficiently estimate the clutter second-order statistics using subspace methods, such as Multiple Signal Classification (MUSIC) [41]. As it is customary in radar literature, the sensing observations are collected in the cube $\mathbf{Y} = \{\{\mathbf{y}_{1,v}, \dots, \mathbf{y}_{I,v}\}\}_{\forall v} \in \mathbb{C}^{M_{BS} \times I \times V}$. The next step would be applying a target cleaning method, such as constant false alarm rate masking [42] or GoDec [43], to erase the targets from \mathbf{Y} , thereby avoiding their identification as part of the clutter. However, under the assumption that δ_{cl}^2 far exceeds all α_t^2 , the clutter covariances can be estimated without the need for any target cleaning.³ This follows from

²For analytical tractability, δ_{cl}^2 , ς_{sp} , ς_D , and ς_τ are assumed to be known. These quantities can be reliably estimated from target-free range-Doppler bins; thus, this assumption does not limit the practical applicability of the proposed pipeline.

³It is important to note that, in the presence of non-homogeneous clutter, the texture may drop below a target's amplitude in its vicinity, making target cleaning necessary. We reserve the investigation of this scenario for future work.

the fact that a target echo is point-like and thus contributes only a rank-one component to the received data, whereas clutter is spatially and temporally extended, occupying multiple range-Doppler bins with significantly higher power [44]. As a result, the sample covariance matrix is dominated by the clutter subspace, and the target contribution appears only as a small rank-one perturbation, to which MUSIC is known to be robust [45]. The spatial sample covariance is computed as

$$\mathcal{B}_{sp} = \mathcal{U}_1(\bar{\mathbf{Y}})\mathcal{U}_1(\bar{\mathbf{Y}})^H / IV - \sigma^2 \mathbf{I}_{M_{BS}} \in \mathbb{C}^{M_{BS} \times M_{BS}}. \quad (38)$$

The MUSIC pseudo-spectrum of the s -th stream is then computed as

$$P_{sp}(\psi) = 1/\mathbf{a}(\psi)^H \mathbf{\Gamma}_{sp} \mathbf{\Gamma}_{sp}^H \mathbf{a}(\psi), \quad (39)$$

where $\mathbf{\Gamma}_{sp} = [\boldsymbol{\lambda}_{sp,1}, \dots, \boldsymbol{\lambda}_{sp,M_{BS}-L}] \in \mathbb{C}^{M_{BS} \times M_{BS}-L}$ contains the eigenvectors associated to the $M_{BS} - L$ weakest eigenvectors of \mathcal{B}_{sp} , i.e., its noise subspace. The peaks of $P(\psi)$ represent the estimated clutter directions, denoted by $\hat{\psi}_n$. By substituting this into (17), we obtain the estimated spatial covariance matrix, denoted as $\hat{\mathbf{B}}_{sp}$. We once again start the estimation of the temporal covariance matrix by computing its sample counterpart, that is

$$\mathcal{B}_t = \mathcal{U}_2(\bar{\mathbf{Y}})\mathcal{U}_2(\bar{\mathbf{Y}})^H / M_{BS}V - \sigma^2 \mathbf{I}_I \in \mathbb{C}^{I \times I}. \quad (40)$$

The MUSIC pseudospectrum is computed in the same way, that is $P_t(f_D) = 1/\mathbf{b}(f_D)^H \mathbf{\Gamma}_t \mathbf{\Gamma}_t^H \mathbf{b}(f_D)$. Then, the peaks of this pseudospectrum are substituted into (20) to obtain $\hat{\mathbf{B}}_t$. The frequency sample covariance matrix is once again defined as

$$\mathcal{B}_f = \mathcal{U}_3(\bar{\mathbf{Y}})\mathcal{U}_3(\bar{\mathbf{Y}})^H / M_{BS}I - \sigma^2 \mathbf{I}_V \in \mathbb{C}^{V \times V} \quad (41)$$

The median range of each patch can be estimated through MUSIC; however, the presence of the diffusive component $\tilde{\mathbf{B}}_f$ might hinder the subspace orthogonality needed by MUSIC. Therefore, we adopt a diffusive-unaware approach and later assess the impact of $\tilde{\mathbf{B}}_f$ on the whole estimation process. The frequency MUSIC pseudo-spectrum is $P_f(r) = 1/\mathbf{d}(2r/c)^H \mathbf{\Gamma}_f \mathbf{\Gamma}_f^H \mathbf{d}(2r/c)$.

B. Clutter-Aware Matched Filtering

We now need to perform MF to eliminate the influence of the transmitted symbols on the radar channel. Let us redefine vector $\boldsymbol{\mu}_{i,v}$ defined in (12) as $\boldsymbol{\mu}_{i,v} = \mathbf{\Phi}_{i,v} \mathbf{x}_{i,v}$. Here the matrix $\mathbf{\Phi}_{i,v} = [\phi_{i,v,1}, \dots, \phi_{i,v,S}] \in \mathbb{C}^{M_{BS} \times S}$ represents the precoded radar channel and is defined as

$$\mathbf{\Phi}_{i,v} = [\mathbf{G}_{i,v} \mathbf{f}_{i,v,1} \sqrt{\rho_{i,v,1}}, \dots, \mathbf{G}_{i,v} \mathbf{f}_{i,v,S} \sqrt{\rho_{i,v,S}}]. \quad (42)$$

By looking at the structure of $\boldsymbol{\mu}_{i,v}$, we see that MF can be readily applied by right-multiplying $\mathbf{y}_{i,v}$ with $\mathbf{x}_{i,v}^\dagger$; however, this does not suppress the clutter action. Thanks to its low-rank structure, the clutter influence can be suppressed through whitening [46], [47]. More specifically, the data cube \mathbf{Y} and the symbol cube $\mathbf{X} = \{\{\mathbf{x}_{1,v}, \dots, \mathbf{x}_{I,v}\}\}_{\forall v}$ are whitened along their time and frequency dimensions: the space dimension is left unwhitened to prevent the accidental target cancellation.

The whitening matrices are the inverse square root of the noise-adjusted covariance matrices, defined as

$$\mathbf{\ddot{B}}_t^{-\frac{1}{2}} = \mathbf{U}_t(\mathbf{\Sigma}_t + \sigma^2 \mathbf{I}_I)^{-\frac{1}{2}} \mathbf{U}_t^H, \quad (43)$$

$$\mathbf{\ddot{B}}_f^{-\frac{1}{2}} = \mathbf{U}_f(\mathbf{\Sigma}_f + \sigma^2 \mathbf{I}_V)^{-\frac{1}{2}} \mathbf{U}_f^H, \quad (44)$$

where $\mathbf{U}_t, \mathbf{\Sigma}_t (\mathbf{U}_f, \mathbf{\Sigma}_f)$ denote the eigen decomposition of $\widehat{\mathbf{B}}_t (\widehat{\mathbf{B}}_f)$. As it was previously mentioned, the Kronecker-separable structure allows for applying whitening independently along each dimension, that is

$$\mathbf{Y}' = \mathcal{F}_2 \left(\mathcal{U}_2(\mathbf{Y}) \mathbf{\ddot{B}}_t^{-\frac{1}{2}} \right), \quad \mathbf{Y}'' = \mathcal{F}_3 \left(\mathcal{U}_3(\mathbf{Y}') \mathbf{\ddot{B}}_f^{-\frac{1}{2}} \right). \quad (45)$$

After applying the same procedure to \mathbf{X} , thus obtaining \mathbf{X}'' , the precoded radar channel is estimated as $\widehat{\mathbf{\Phi}}_{i,v} = [\widehat{\phi}_{i,v,1}, \dots, \widehat{\phi}_{i,v,S}] = \{\mathbf{Y}''\}_{i,v} \{\mathbf{X}''\}_{i,v}^\dagger$.

C. Range-Angle and Range-Velocity Maps

The next step in the radar signal processing pipeline is the computation of RA and RV maps, whose peaks shall reveal the estimated values of each target parameter. We thus compute the range profile by applying a discrete Fourier transform (DFT) along the frequency dimension on the estimated radar channels. The range profile of the v' -th range bin is then computed as

$$\mathbf{r}_{i,v',s} = \sum_{v=1}^V e^{-\frac{j2\pi vv'}{V'}} \widehat{\phi}_{i,v,s} \in \mathbb{C}^{M_{BS}}, \quad (46)$$

where $v' \in [1, V']$ and $V' \geq V$, accounting for zero padding. The delay of each target is quantized with a resolution of $1/\Delta_f V'$. The angle profiles associated with each range profile are then computed through MUSIC. We thus compute the sample covariance matrix of each bin's range profile as

$$\mathbf{Q}_{v',s} = \frac{1}{I} \sum_{i=1}^I \mathbf{r}_{i,v',s} \mathbf{r}_{i,v',s}^H \in \mathbb{C}^{M_{BS} \times M_{BS}}. \quad (47)$$

Similarly to (39), let us denote with $\mathbf{\Gamma}_{v',s}$ the noise subspace of $\mathbf{Q}_{v',s}$, then the angular profile of the v' -th bin is $P_{s,v'}(\theta) = 1/\mathbf{a}(\theta)^H \mathbf{\Gamma}_{v',s} \mathbf{\Gamma}_{v',s}^H \mathbf{a}(\theta)$. The next step is to compute the velocity profile associated with each range bin. We first project each range profile onto the angle with the highest MUSIC power within that range bin, denoted by $\theta_{v'}^M$. Then, an inverse DFT is applied to each column of this matrix

$$q_{i',v',s} = \sum_{i=1}^I e^{\frac{j2\pi ii'}{I'}} \mathbf{a}(\theta_{v'}^M)^H \mathbf{r}_{i,v',s}. \quad (48)$$

By collecting all the $q_{i',v',s}$ into a matrix, the RV map gets associated with the s -th stream $\mathbf{V}_s \in \mathbb{C}^{I' \times V'}$, where $I' \geq I$ accounts for zero padding.

VI. PRECODING STRATEGIES

In this section, we will present the precoding strategies adopted by the system. We assume that all the subcarriers within the same coherence block have the same precoding matrix. We'll thus drop the subcarrier index from the subsequent derivations and derive the precoding matrix of an arbitrary block. During pilot transmission, the system does

Table I: Simulation parameters default values

Parameter	value
BS antennas (M_{BS})	32
UE antennas (M_{UE})	2
Active subcarriers (V)	1000
Number of transmission streams (S)	3
Number of subcarriers used for ch. estimation (τ_p)	3
Subcarrier spacing (Δ_f)	20 kHz
N ^o of coherent subcarriers (V_{cho})	20
Cyclic prefix duration (T_{cp})	1 μ s
N ^o of sensing OFDM symbols (I)	1000
Carrier frequency (f_c)	2 GHz
UE's clusters angular spread (ς_k)	1 ^o
UE's channel gain (α_k)	-70 dB
Clutter patches angular spread (ς_{sp}^2)	2 ^o
Clutter patches delay spread (ς_d^2)	1 ns
N ^o of time-coherent clutter observations (I_c)	1000
$\widetilde{\mathbf{B}}_f$ frequency correlation decay base (μ_f)	0.9
$\widetilde{\mathbf{B}}_f$ coherence bandwidth (B_{cho})	50 kHz
$\widetilde{\mathbf{B}}_f$ power coefficient (χ)	0 dB
UE/radar noise's powers (σ_k^2/σ^2)	-160 dB.
Total power budget (P_{Tx})	32 dBm
Power trade-off coefficient (γ)	0.5
Targets' RCSs powers ($\delta_{Tg,l}^2$)	5, 1 dBsm
Clutter's texture (δ_{cl}^2)	-133 dB
Radiative elements gains (G_{Tx}, G_{Rx})	0 dBi
Zero-padded version of I, V (I', V')	3000, 3000

not have CSIT, or rather assumes that the $\widehat{\mathbf{h}}_{i,k}$ at the end of the previous frame has drifted too far from its actual value. For this reason, during pilot slots, the BS relies solely on the second-order statistics of $\mathbf{h}_{i,k}$, enabling eigen-beamforming [48]. Indeed, the n -th largest eigenvalue of $\mathbf{C}_{Tx,k}$ shall be denoted by $\mathbf{u}_{Tx,k,n}$. When the UE feeds back the channel estimates $\widehat{\mathbf{H}}_{i,k}$ to the transmitter, thus making CSIT available, the BS employs MMSE precoding [49, Ch. 5]. Let us collect all the pilot slot indices in the set \mathcal{P} , then the precoding matrix for UE k is defined as

$$\mathbf{F}_{i,k} = \begin{cases} [\mathbf{u}_{Tx,k,1}, \dots, \mathbf{u}_{Tx,k,M_{UE}}] & \text{if } i \in \mathcal{P}, \\ \mathbf{T}_i^{-1} \alpha_k \widehat{\mathbf{H}}_{i,k}^\top & \text{otherwise,} \end{cases} \quad (49)$$

where $\mathbf{T}_i = \sum_{k=1}^K (\alpha_k^2 \widehat{\mathbf{H}}_{i,k}^\top \widehat{\mathbf{H}}_{i,k}^* + \widetilde{\mathbf{\Xi}}_{i,k}) + \sigma_k^2 \mathbf{I}_{M_{BS}}$. Here $\widetilde{\mathbf{\Xi}}_{i,k} \in \mathbb{C}^{M_{BS} \times M_{BS}}$ is obtained by summing all the $M_{BS} \times M_{BS}$ blocks along the main diagonal of $\widetilde{\mathbf{\Xi}}_{i,k}$. The sensing beam definition is not dependent on whether i is a data or pilot slot: we are adopting a beam-sweeping strategy, discretizing the sensing interval $[\theta_{start}, \theta_{end}]$ into $\{\theta_i\}_{i=1}^I$. The interference between the sensing stream and the communication ones must be eliminated; therefore, if some degree of CSIT is available, the sensing beams must be projected onto the null space of the communication channels, thus defining the sensing precoding vector as

$$\mathbf{f}_{i,v,s} = \begin{cases} \mathbf{a}(\theta_i) & \text{if } i \in \mathcal{P}, \\ (\mathbf{I}_M - \widehat{\mathbf{H}}_i^\dagger \widehat{\mathbf{H}}_i) \mathbf{a}(\theta_i) & \text{otherwise,} \end{cases} \quad (50)$$

where $\widehat{\mathbf{H}}_i = [\alpha_1 \widehat{\mathbf{H}}_{i,1}^\top, \dots, \alpha_K \widehat{\mathbf{H}}_{i,K}^\top]^\top \in \mathbb{C}^{K M_{UE} \times M_{BS}}$.

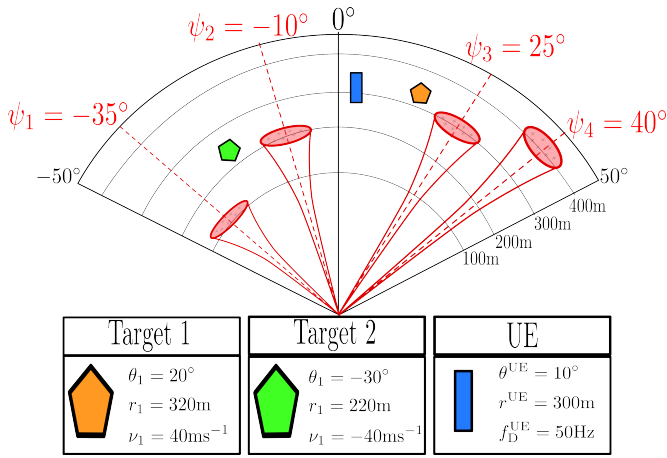


Fig. 5: Simulated scenario with $L = 2$ radar targets, $N = 4$ clutter patches and a single communication UE.

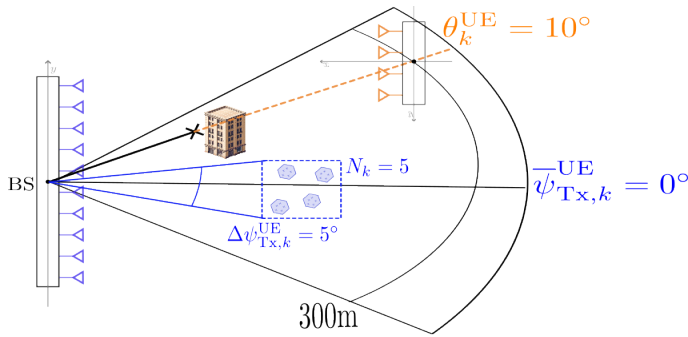


Fig. 6: Zoomed-in geometric layout of the BS-UE communication channel, where the clustered multipath fading is made of 5 clusters. Notice that the set of clusters constituting the multipath fading of \mathbf{h}_k does not constitute a clutter cluster, as their RCSs are assumed to be too low and thus they only contribute to \mathbf{C}_k .

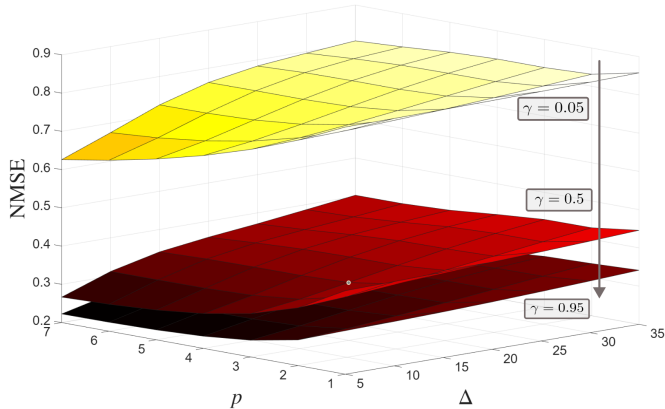


Fig. 7: 3D plot of the channel estimation NMSE performance vs the pilot spacing Δ and the number of previous pilot observations p used in the channel estimation. Each surface has been obtained with a different γ power coefficient, highlighting the trade-off between sensing and communication.

VII. NUMERICAL RESULTS

The effects of channel aging on channel estimation and the proposed radar pipeline are numerically evaluated in the scenario depicted in Figs. 5 and 6. The said figures also report the default values of the simulation parameters, the rest of which are listed in Table II. The simulations assume the presence of

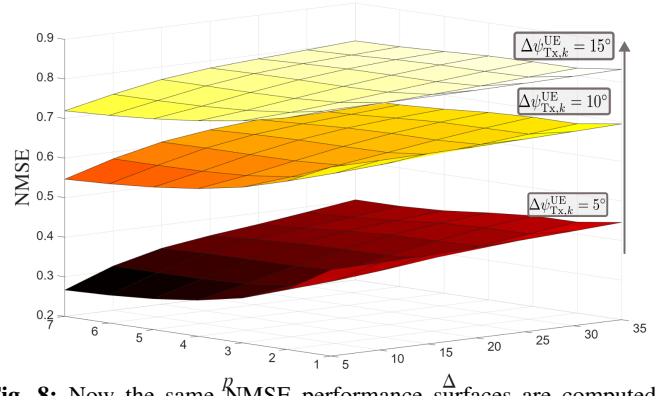


Fig. 8: Now the same \hat{N} MSE performance surfaces are computed for different values of $\Delta\psi_{\text{Tx},k}^{\text{UE}}$. We can see that the distance between clusters is directly proportional to the NMSE.

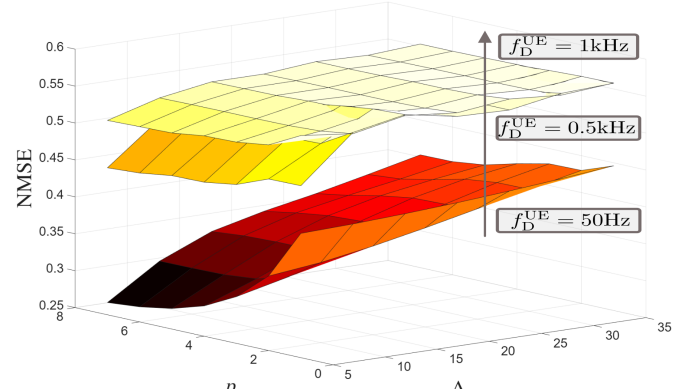


Fig. 9: NMSE surfaces computed for different values of UE's doppler shift f_D^{UE} . As the UE's mobility increases, the surfaces become progressively flatter due to the rapid decorrelation between pilot slots.

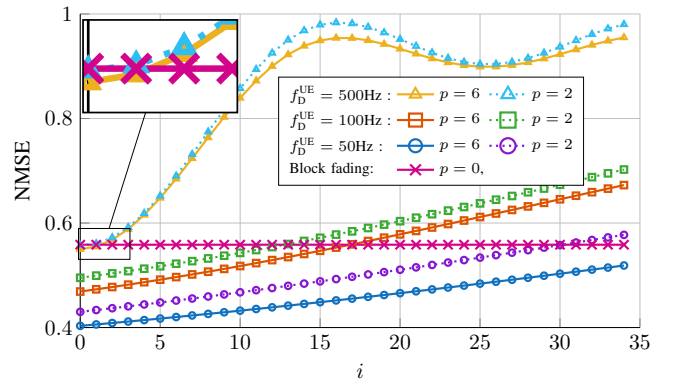


Fig. 10: NMSE progression within a frame of $\Delta = 35$ data slots. We see that the UE mobility has a much bigger impact than p .

a single UE. Since $K = 1$, the index k will be omitted in the following considerations. We assume that the BS employs equal power allocation between streams and subcarriers, that is $\rho_{i,v} = \left[\sqrt{\frac{P_{\text{comm}}}{M_{\text{UE}}KV}}, \dots, \sqrt{\frac{P_{\text{comm}}}{M_{\text{UE}}KV}}, \sqrt{\frac{P_{\text{sens}}}{V}} \right] \in \mathbb{C}^S, \forall i, v$.

A. Communication Channel Estimation

We start by analyzing the UE's DL channel estimation process, described in Lemma 5. The channel \mathbf{h}_k is estimated during pilot slots. This estimate depends on the frame size, Δ . The channel estimate in Corollary 1 is computed using p previous pilot observations, thereby leveraging the channel's

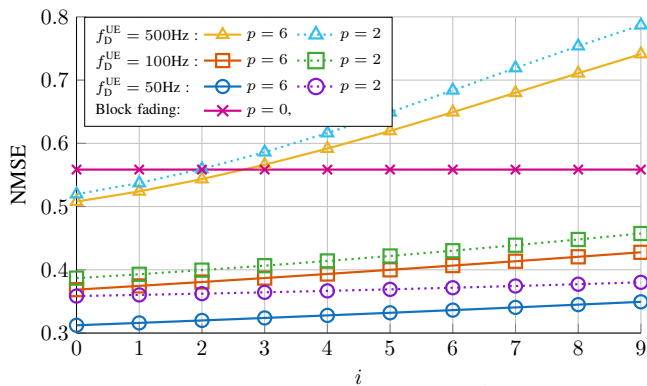


Fig. 11: The same NMSE progression, now with $\Delta = 10$. p now has a bigger impact on the NMSE, and this is due to the smaller frame dimension.

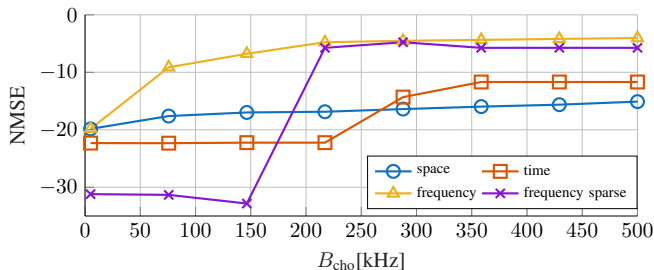


Fig. 12: Clutter estimation NMSE as a function of B_{cho}

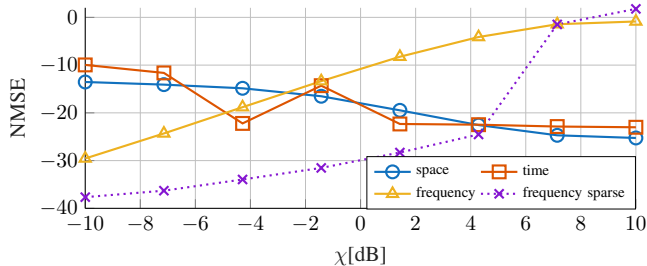


Fig. 13: Clutter estimation NMSE as a function of χ

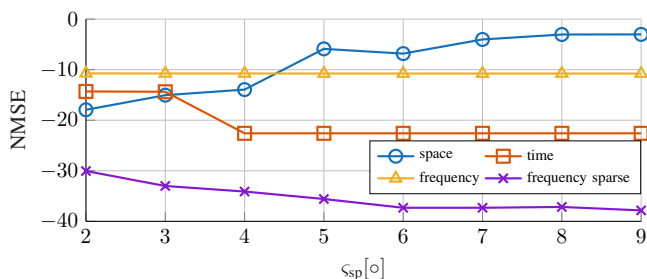


Fig. 14: Clutter estimation NMSE as a function of ζ_{sp}

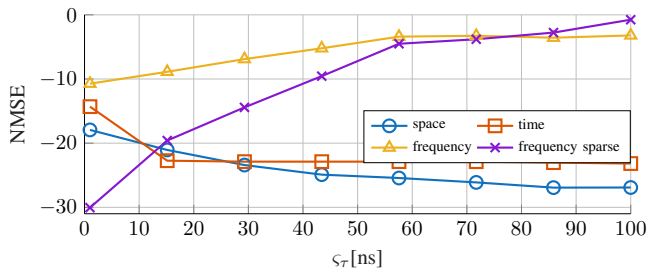


Fig. 15: Clutter estimation NMSE as a function of ζ_{τ}

known time-correlation structure. \mathbf{C}_k has been normalized to $\text{Tr}(\mathbf{C}_k) = 1$, allowing for a cleaner SNR expression. The UE's

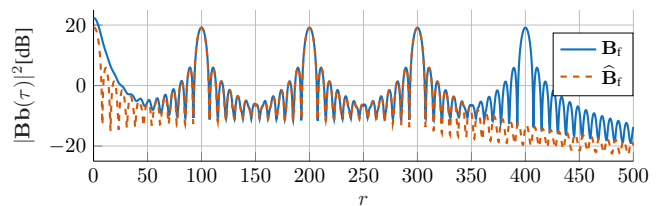


Fig. 16: beampattern of \mathbf{B}_f and $\hat{\mathbf{B}}_f$ with $B_{cho} = 500\text{kHz}$

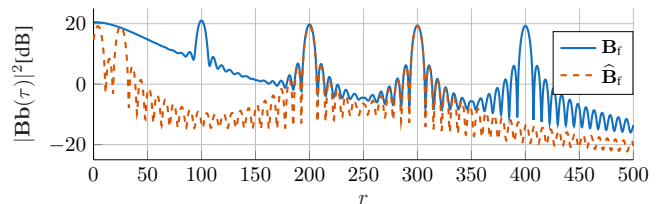


Fig. 17: beampattern of \mathbf{B}_f and $\hat{\mathbf{B}}_f$ with $\chi = 8\text{dB}$

communication SNR is equal to $\text{SNR}_{\text{UE}} = \frac{\alpha_k^2 P_{\text{comm}}}{\sigma_k^2} = 21 + 10 \log_{10}(\gamma)$ dB. The metric chosen to assess the channel estimation quality is the normalized mean squared error (NMSE), defined as $\text{NMSE}_{i,k} = \text{Tr}(\tilde{\mathbf{\Xi}}_{i,k})$. We first investigate the channel estimation performance during a generic pilot slot: Fig. 7-9 shows 3D surfaces with Δ on the x axis, p on the y axis, and the NMSE on the z axis. Fig. 7 is a visual representation of the sensing-communication trade-off, as a higher γ corresponds to a lower NMSE. This hardly comes as a surprise since γ represents the fraction of power dedicated to the communication beams. Interestingly, the performance gap between $\gamma = 0.05$ and $\gamma = 0.5$ is much higher than the gap between the latter and $\gamma = 0.95$. Fig. 8 shows the impact of $\Delta\psi_{\text{BS},k,n}$ onto the NMSE. The NMSE degradation is proportional to $\Delta\psi_{\text{BS},k,n}$ is caused by the fact that a greater distance between clusters makes the reflection process more diffusive than specular.

Next, we analyze the NMSE dependence on the UE's mobility, measured through its Doppler shift: Fig. 9 shows that higher mobility implies a performance loss, but, more interestingly, a loss in sensitivity to Δ and p , as the NMSE surfaces become progressively flatter with f_D^{UE} . This is caused by the rapid decorrelation induced by high mobility, which ultimately makes the estimator defined in Lemma 5 collapse onto a standard block fading MMSE estimator. Indeed, a block fading estimator is obtained from Lemma 5 by setting $p = 0$. Our investigation continues with Fig. 10 and Fig. 11: within the frame, the estimate drifts away from the real channel value, causing the NMSE to increase with i .

It goes without saying that the block fading NMSE does not change along the frame. These figures show exactly when our approach outperforms a block fading one. Indeed, a block fading model is the better alternative when UEs have too high a Doppler shift compared to when Δ is big. By reducing Δ when UEs show high Doppler, our channel estimator dramatically outperforms block fading. It is worth mentioning that reducing Δ would inevitably reduce the UEs' SE. We reserve a careful investigation of SE for future work, even though a trade-off between channel estimation accuracy, inversely proportional to Δ , and the fraction of data slots in the frame is expected to manifest itself [14].

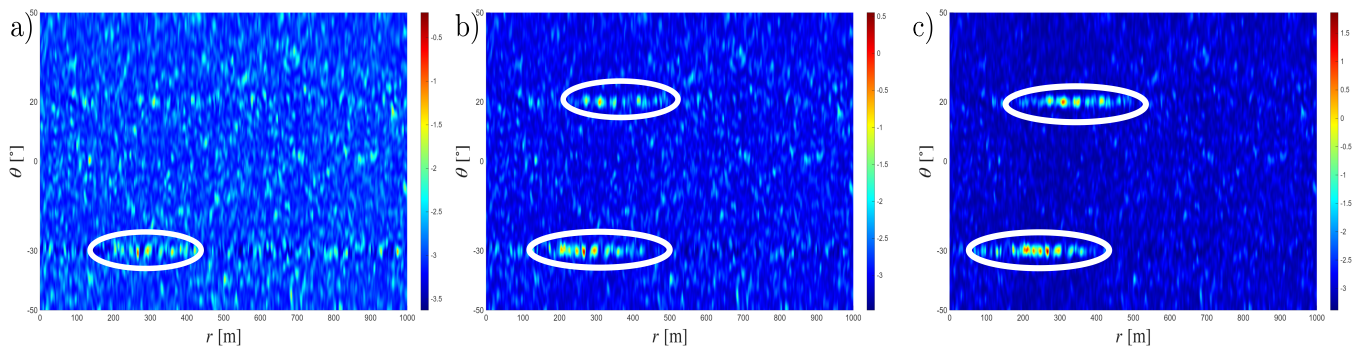


Fig. 18: Range-angle map in dB scale associated with the first communication stream, i.e., $s = 1$, for different levels of γ , more specifically: a) $\gamma = 0.05$, b) $\gamma = 0.5$, and c) $\gamma = 0.95$. We have subtracted 80% of their first singular value from these maps to have a clearer map. This partially removes the horizontal stripe across r , which indicates energy leakage across range due to the high signal-to-noise ratio (SNR) of the targets.

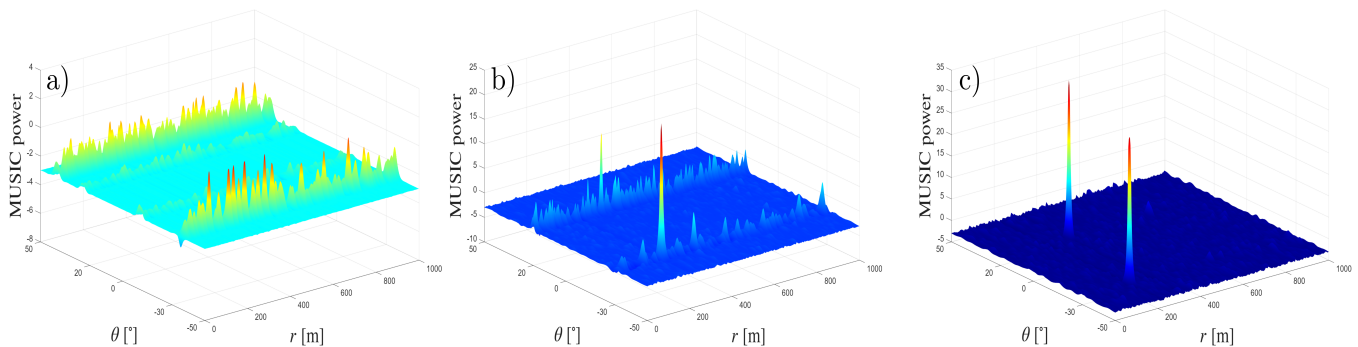


Fig. 19: Range-angle map in dB scale associated with the sensing stream, i.e., $s = S$, for different levels of clutter awareness, that is: a) MF without whitening, b) MF with the estimated covariances, and c) MF with the true covariances. We have implemented the same singular value subtraction as well as a Kaiser window [50] of 3rd order.

B. Clutter Estimation

We now move over to evaluating the performance of the clutter covariance estimation method proposed in Section V-A. Once again the performance metric is the NMSE between the estimated covariance matrix and the actual one, which is defined as $\text{NMSE}_x = \|\hat{\mathbf{B}}_x - \mathbf{B}_x\|_F^2 / \|\mathbf{B}_x\|_F^2$. A particular mention goes to the NMSE labeled “Freq.sparse”, which measures how well MUSIC can capture $\bar{\mathbf{B}}_f$, since it is defined as $\text{NMSE}_{f.\text{ sparse}} = \|\hat{\mathbf{B}}_f - \bar{\mathbf{B}}_f\|_F^2 / \|\bar{\mathbf{B}}_f\|_F^2$. Our numerical results related to clutter estimation are obtained by averaging 15 independent \mathbf{Y} . Starting from Fig. 12, we see that a high B_{cho} greatly hinders both frequency NMSEs. The source of this error is shown in Fig. 16, where the beampattern of the estimated frequency covariance matrix is compared against the true one. Here we can see that the diffusive covariance component induces an exponential decay from $r = 0$: when B_{cho} is high, this decay becomes very sharp, so sharp that MUSIC confuses it for a peak originated by a clutter cluster. A similar behavior can be seen in Fig. 17: as χ increases, the exponential decay induced by $\bar{\mathbf{B}}_f$ becomes more prominent, thereby causing MUSIC to identify false peaks around $r = 0$. The frequency-NMSE degradation induced by an increasing χ can be seen in Fig. 13. Here, we can observe that both frequency NMSEs follow the same trend, sharply rising from -30 dB and converging around 0 dB. Interestingly, clutter with a more prominent surface roughness and multipath appears to

be beneficial for estimating \mathbf{B}_{sp} and \mathbf{B}_t , as evidenced by the decrease in their NMSEs with χ . Lastly, Figs. 14 and 15 show the NMSE progression as a function of the clutter patches’ angular and delay spreads, respectively. We observe that, as said spreads increase, the NMSE associated with that component (i.e., the space and frequency NMSEs, respectively) increases as well. This is to be expected as a larger spread corresponds to less orthogonal clusters, in turn spoiling the functioning of MUSIC as it relies on said orthogonality. However, it is interesting to notice the interplay between components: Fig. 14 shows how an increased ς_{sp} is beneficial for the estimation of \mathbf{B}_t and $\bar{\mathbf{B}}_f$. A dual behavior is seen in 15, since an increase in delay spread makes the time and space NMSE decrease. It is also worth mentioning that, as I_c increases, the time NMSE sharply decreases until converging around -30 dB. This has not been given a dedicated figure due to space constraints. These so-called cross-contamination effects are interesting because, while it is true that the value of the parameters shown in Fig. 12-15 are set by nature, they are not immune to the observer effect of the BS. For instance, allocating more antennas to the receiving array of the BS may decrease the observed angular spread: within this frame, the previous figures become a sort of usage manual, explaining the consequence of increasing or decreasing a clutter parameter.

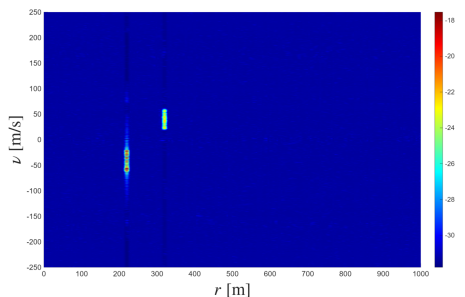


Fig. 20: Range velocity associated with the sensing stream, obtained using MF with the estimated covariances. Note that the same SV subtraction applied to the RA map has been applied to this one, together with a noise floor subtraction.

C. Range Maps

We now move over to the assessment of the radar performance by showing how the RA and RV look, more importantly, comparing the look of the maps associated with the stream with $s = 1$, which shall be referred to as the communication stream, and the ones associated with the sensing stream. We start with Fig. 18, which shows how the RA map associated with the communication stream looks for different values of the power trade-off parameter γ . This figure shows that increasing γ does give some benefits: there is indeed a steady quality improvement between 18a, 18b, and 18c. We observe that, while these maps offer a good angular resolution, they lack range resolution. Indeed 18b and 18c show that there is a semblance of range information, highlighted by the white circles, as the "peaks" are vaguely centered around the target's true ranges; however, said peaks are way too large to be of any use. This is an important result as it tells us that if massive MIMO precoding techniques are employed, dedicated sensing beams are unavoidable. This is ascribed to the fact that massive MIMO precoding vectors do not have any notion of directionality, a notion that we find in a beamsweeping precoder. This makes them suitable for guaranteeing high SE to the UEs, while they cannot be used for radar purposes. Indeed, we see a dramatically different situation in Fig. 19, which shows the RA map associated with the sensing stream in different MF regimes. Note that the impact of γ on these RA maps has not been investigated, as they are much more robust to power changes due to the directionality of the precoder and the high SNR per stream here simulated. Fig. 19a shows that ignoring the presence of clutter leads to unusable maps, as said maps only present horizontal stripes in correspondence with the clutter directions. The impact of clutter awareness is evident in Fig. 19b, where we have applied MF using the estimated covariances. As a result, the map appears clean, albeit with the presence of horizontal stripes.⁴ When the true covariance matrix is employed, we see that the horizontal stripes become almost perfectly canceled by the singular value (SV) subtraction, and the peaks have sensibly higher power. The RV maps for Fig. 19b and Fig. 19c are shown in Fig. 20 and Fig. 21; the RV maps associated with the other previously presented RA maps have been omitted as they look like noise

⁴The horizontal stripes are caused by the fact that the targets have a high SNR, thus their energy spreads across range bins. However, the peak is 10 dB higher than this stripe, so this does not constitute a source of confusion.

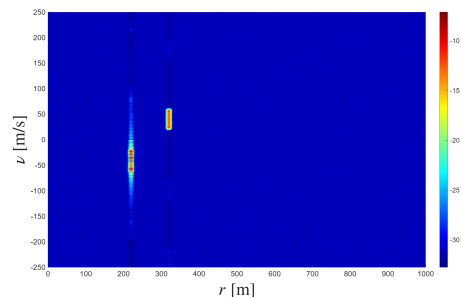


Fig. 21: Range velocity associated with the sensing stream, obtained using MF with the true covariance

floors without any discernible trend. Fig. 20 and Fig. 21 confirm the trend of Fig. 20 and Fig. 19, where using the true covariance in the MF process gives rise to sensibly higher peaks. Interestingly, we see that the first target's peak (in v) is wider in Fig. 21 than in Fig. 20.

VIII. CONCLUSIONS

This paper examined a multi-user multiple input multiple output (MU-MIMO) OFDM ISAC network that concurrently serves multiple UEs and performs monostatic sensing. The temporal evolution of the propagation environment was shown to induce channel aging, motivating the development of an aging-aware channel estimator, as well as Doppler-affected clutter. The clutter's structure enabled us to develop a novel radar pipeline, which facilitates the estimation of multiple target positions in a clutter-dominated environment. Said pipeline's low complexity makes it possible to be deployed on ISAC-capable BSs operating in the presence of urban clutter, a scenario for which Kronecker-separability holds. Our results show that, in low-to-moderate mobility regimes, reliance on a block-fading model leads to substantial performance degradation compared to aging-aware estimation. Moreover, we have shown that under reasonable assumptions, structured clutter can be effectively modeled and mitigated, enabling more accurate evaluation of ISAC performance. As part of future work, we plan on extending this model to multi-static ISAC scenarios, where the sensing geometry is more complex and perfect knowledge of the transmitted symbol is not always guaranteed. Furthermore, non-homogeneous clutter models will be investigated.

REFERENCES

- [1] F. Liu, Y. Cui, C. Masouros, J. Xu, T. X. Han, Y. C. Eldar, and S. Buzzi, "Integrated sensing and communications: Towards dual-functional wireless networks for 6G and beyond," *IEEE journal on selected areas in communications*, 2022.
- [2] N. Babu, C. Masouros, C. B. Papadias, and Y. C. Eldar, "Precoding for multi-cell ISAC: From coordinated beamforming to coordinated multipoint and bi-static sensing," *IEEE Transactions on Wireless Communications*, vol. 23, no. 10, pp. 14 637–14 651, 2024.
- [3] M. F. Keskin, F. Jiang, F. Munier, G. Seco-Granados, and H. Wymeersch, "Optimal spatial signal design for mmwave positioning under imperfect synchronization," *IEEE Transactions on Vehicular Technology*, vol. 71, no. 5, pp. 5558–5563, 2022.
- [4] X. Fang, W. Feng, Y. Chen, N. Ge, and Y. Zhang, "Joint communication and sensing toward 6G: Models and potential of using MIMO," *IEEE Internet of Things Journal*, vol. 10, no. 5, pp. 4093–4116, 2023.

- [5] S. Rivetti, E. Björnson, and M. Skoglund, "Secure spatial signal design for isac in a cell-free mimo network," in *2024 IEEE Wireless Communications and Networking Conference (WCNC)*. IEEE, 2024, pp. 01–06.
- [6] A. Liu, Z. Huang, M. Li, Y. Wan, W. Li, T. X. Han, C. Liu, R. Du, D. K. P. Tan, J. Lu, Y. Shen, F. Colone, and K. Chetty, "A survey on fundamental limits of integrated sensing and communication," *IEEE Communications Surveys & Tutorials*, vol. 24, no. 2, pp. 994–1034, 2022.
- [7] F. Liu, Y.-F. Liu, Y. Cui, C. Masouros, J. Xu, T. X. Han, S. Buzzi, Y. C. Eldar, and S. Jin, "Sensing with communication signals: From information theory to signal processing," *IEEE Journal on Selected Areas in Communications*, pp. 1–1, 2025.
- [8] M. U. Baig, J. Vinogradova, G. Fodor, and C. Mollén, "Joint communication and sensing beamforming for passive object localization," in *WSA and SCC 2023; 26th Int. ITG Workshop on Smart Antennas and 13th Conf. on Systems, Communications, and Coding*, 2023, pp. 1–6.
- [9] S. Rivetti, O. T. Demir, E. Björnson, and M. Skoglund, "Clutter-aware target detection for ISAC in a millimeter-wave cell-free massive MIMO system," *arXiv preprint arXiv:2411.08759*, 2024.
- [10] M. B. Salman, Ö. T. Demir, and E. Björnson, "When are sensing symbols required for isac?" *IEEE Transactions on Vehicular Technology*, vol. 73, no. 10, pp. 15709–15714, 2024.
- [11] K. T. Truong and R. W. Heath, "Effects of channel aging in massive MIMO systems," *Journal of Communications and Networks*, vol. 15, no. 4, pp. 338–351, 2013.
- [12] G. Fodor, J. Vinogradova, P. Hammarberg, K. K. Nagalapur, Z. T. Qi, H. Do, R. Blasco, and M. U. Baig, "5G new radio for automotive, rail, and air transport," *IEEE Communications Magazine*, vol. 59, no. 7, pp. 22–28, 2021.
- [13] C. Kong, C. Zhong, A. K. Papazafiroopoulos, M. Matthaiou, and Z. Zhang, "Sum-rate and power scaling of massive mimo systems with channel aging," *IEEE transactions on communications*, vol. 63, no. 12, pp. 4879–4893, 2015.
- [14] S. Fodor, G. Fodor, D. Gürgünoğlu, and M. Telek, "Optimizing pilot spacing in MU-MIMO systems operating over aging channels," *IEEE Transactions on Communications*, vol. 71, no. 6, pp. 3708–3720, 2023.
- [15] S. Daei, G. Fodor, M. Skoglund, and M. Telek, "Toward optimal pilot spacing and power control in multi-antenna systems operating over non-stationary Rician aging channels," *IEEE Transactions on Communications*, vol. 73, no. 6, pp. 3761–3777, 2025.
- [16] E. Björnson, M. Matthaiou, and M. Debbah, "Massive MIMO with non-ideal arbitrary arrays: Hardware scaling laws and circuit-aware design," *IEEE Transactions on Wireless Communications*, vol. 14, no. 8, pp. 4353–4368, 2015.
- [17] J. Yuan, H. Q. Ngo, and M. Matthaiou, "Machine learning-based channel prediction in massive MIMO with channel aging," *IEEE Transactions on Wireless Communications*, vol. 19, no. 5, pp. 2960–2973, 2020.
- [18] J. Chen, X. Wang, and Y.-C. Liang, "Impact of channel aging on dual-function radar-communication systems: Performance analysis and resource allocation," *IEEE Transactions on Communications*, vol. 71, no. 8, pp. 4972–4987, 2023.
- [19] H. Luo, F. Gao, H. Lin, S. Ma, and H. V. Poor, "Yolo: An efficient terahertz band integrated sensing and communications scheme with beam squint," *IEEE Transactions on Wireless Communications*, vol. 23, no. 8, pp. 9389–9403, 2024.
- [20] Q. Lu, K. Yang, Z. Zhang, and T.-K. Truong, "Mimo ofdm robust transceiver design for clutter suppression in isac systems," *IEEE Transactions on Vehicular Technology*, 2025.
- [21] J. Vinogradova and G. Fodor, "On target detection in the presence of clutter in joint communication and sensing cellular networks," in *2023 16th International Conference on Signal Processing and Communication System (ICSPCS)*, 2023, pp. 01–10.
- [22] Ö. T. Demir and E. Björnson, "RIS-assisted ISAC: Precoding and phase-shift optimization for mono-static target detection," *arXiv preprint arXiv:2410.06855*, 2024.
- [23] K. Greenewald, E. Zelnio, and A. H. Hero, "Robust SAR STAP via Kronecker decomposition," *IEEE Transactions on Aerospace and Electronic Systems*, vol. 52, no. 6, pp. 2612–2625, 2016.
- [24] J. Ward, "Space-time adaptive processing for airborne radar," in *IEE Colloquium on Space-Time Adaptive Processing*. IET, 1998, pp. 2–1.
- [25] T. L. Marzetta and H. Yang, *Fundamentals of massive MIMO*. Cambridge University Press, 2016.
- [26] S. Daei, M. Skoglund, and G. Fodor, "Improved downlink channel estimation in time-varying FDD massive MIMO systems," in *2024 IEEE 25th International Workshop on Signal Processing Advances in Wireless Communications (SPAWC)*. IEEE, 2024, pp. 571–575.
- [27] S. D. Liyanaarachchi, T. Riihonen, C. B. Barneto, and M. Valkama, "Joint mimo communications and sensing with hybrid beamforming architecture and OFDM waveform optimization," *IEEE Transactions on Wireless Communications*, 2023.
- [28] M. Bengtsson and P. Zetterberg, "Some notes on the Kronecker model," *EURASIP Journal on Wireless Communications and Networking*, 2006.
- [29] 3GPP, "Study on channel model for frequencies from 0.5 to 100 GHz," 3GPP, Technical Specification (TS) 38.901, 09 2025, version 19.1.0.
- [30] K. T. Truong and R. W. Heath, "Effects of channel aging in massive MIMO systems," *Journal of Communications and Networks*, vol. 15, no. 4, pp. 338–351, 2013.
- [31] H. Abeida, "Data-aided snr estimation in time-variant Rayleigh fading channels," *IEEE transactions on signal processing*, vol. 58, no. 11, pp. 5496–5507, 2010.
- [32] M. I. Skolnik, *Radar handbook*. McGraw-Hill, 2008.
- [33] T. Duan, P. Shui, J. Wang, and S. Xu, "Analytical coherent detection in high-resolution dual-polarimetric sea clutter with independent inverse gamma textures," *Remote Sensing*, vol. 16, no. 8, p. 1315, 2024.
- [34] Ö. T. Demir and E. Björnson, "Is channel estimation necessary to select phase-shifts for RIS-assisted massive MIMO?" *IEEE Transactions on Wireless Communications*, vol. 21, no. 11, pp. 9537–9552, 2022.
- [35] A. Abdi and M. Kaveh, "A space-time correlation model for multiple-element antenna systems in mobile fading channels," *IEEE Journal on Selected Areas in communications*, vol. 20, no. 3, pp. 550–560, 2002.
- [36] Ö. T. Demir, E. Björnson, and L. Sanguinetti, "Channel modeling and channel estimation for holographic massive MIMO with planar arrays," *IEEE Wireless Communications Letters*, vol. 11, no. 5, pp. 997–1001, 2022.
- [37] C.-X. Wang and M. Patzold, "Efficient simulation of multiple cross-correlated Rayleigh fading channels," in *14th IEEE Proceedings on Personal, Indoor and Mobile Radio Communications, 2003. PIMRC 2003.*, vol. 2. IEEE, 2003, pp. 1526–1530.
- [38] P. J. Sherman, "On the eigenstructure of the ar (1) covariance," in *2023 IEEE Statistical Signal Processing Workshop (SSP)*. IEEE, 2023, pp. 6–10.
- [39] E. B. Kama, J. Kim, and E. Björnson, "Downlink pilots are essential for cell-free massive MIMO with multi-antenna users," in *2024 IEEE Wireless Communications and Networking Conference (WCNC)*. IEEE, 2024, pp. 1–6.
- [40] Z. He, H. Shen, W. Xu, Y. C. Eldar, and X. You, "MSE-based training and transmission optimization for MIMO ISAC systems," *IEEE Transactions on Signal Processing*, 2024.
- [41] P. Stoica, R. L. Moses *et al.*, *Spectral analysis of signals*. Pearson Prentice Hall Upper Saddle River, NJ, 2005, vol. 452.
- [42] H. Rohling, "Radar CFAR thresholding in clutter and multiple target situations," *IEEE transactions on aerospace and electronic systems*, no. 4, pp. 608–621, 2007.
- [43] T. Zhou and D. Tao, "Godec: Randomized low-rank & sparse matrix decomposition in noisy case," in *Proceedings of the 28th International Conference on Machine Learning, ICML 2011*, 2011.
- [44] M. A. Richards, J. A. Scheer, and W. A. Holm, *Principles of modern radar: basic principles*. IET, 2010.
- [45] P. Stoica and A. Nehorai, "Music, maximum likelihood, and cramer-rao bound," *IEEE Transactions on Acoustics, speech, and signal processing*, vol. 37, no. 5, pp. 720–741, 2002.
- [46] M. Izquierdo, M. Hernandez, O. Graullera, and J. Anaya, "Signal-to-noise ratio enhancement based on the whitening transformation of colored structural noise," *Ultrasonics*, vol. 38, no. 1-8, pp. 500–502, 2000.
- [47] G. Sun, Z. He, F. Jia, and R. Li, "Kronecker product PCA for structured covariance matrix of airborne radar STAP," in *2017 IEEE Radar Conference (RadarConf)*. IEEE, 2017, pp. 1015–1019.
- [48] I. Wajid, Y. C. Eldar, and A. Gershman, "Robust downlink beamforming using covariance channel state information," in *2009 IEEE International Conference on Acoustics, Speech and Signal Processing*. IEEE, 2009, pp. 2285–2288.
- [49] Ö. T. Demir, E. Björnson, L. Sanguinetti *et al.*, "Foundations of user-centric cell-free massive MIMO," *Foundations and Trends® in Signal Processing*, vol. 14, no. 3-4, pp. 162–472, 2021.
- [50] A. V. Oppenheim, *Discrete-time signal processing*. Pearson Education India, 1999.